Available online at www.sciencedirect.com

ScienceDirect

Ceramics International 35 (2009) 1345–1351

CERAMICS INTERNATIONAL

www.elsevier.com/locate/ceramint

Effect of Fe_2O_3 on properties and densification of $Ce_{0.8}Gd_{0.2}O_{2-\delta}$ by PCAS

Ki-Tae Lee [a,b], Dong-Ki Kim [b], Jeong-Hwan Park [a], In-Jin Shon [a,b,*]

[a] *Department of Hydrogen and Fuel Cells Engineering, Specialized Graduate School, Chonbuk National University, 664-14 Deokjin-dong 1-ga, Deokjin-gu, Jeonju, Jeonbuk 561-756, Republic of Korea*

[b] *Division of Advanced Materials Engineering and the Research Center of Industrial Technology, College of Engineering, Chonbuk National University, 664-14 Deokjin-dong 1-ga, Deokjin-gu, Jeonju, Jeonbuk 561-756, Republic of Korea*

Received 5 May 2008; received in revised form 23 May 2008; accepted 22 June 2008
Available online 26 July 2008

Abstract

Dense $Ce_{0.8}Gd_{0.2}O_{2-\delta}$ was sintered by pulsed current activated sintering (PCAS) within 6 min from $Ce_{0.8}Gd_{0.2}O_{2-\delta}$ nanopowder prepared by co-precipitation method. Sintering was accomplished under the combined effects of a pulsed current and mechanical pressure. Highly dense $Ce_{0.8}Gd_{0.2}O_{2-\delta}$ with relative density of up to 96.3% was produced under simultaneous application of an 80-MPa pressure and the pulsed current. The effects of Fe_2O_3 additions on the sintering behavior, ionic conductivities, and mechanical properties of the $Ce_{0.8}Gd_{0.2}O_{2-\delta}$ were investigated.

Keywords: C. Ionic conductivity; C. Mechanical properties; Pulsed current activated sintering; $Ce_{0.8}Gd_{0.2}O_{2-\delta}$; Densification

1. Introduction

Solid oxide fuel cells (SOFCs) systems are very attractive because of two major advantages, high efficiency and very low emission of pollutants. In the past years, intense research work has been conducted in order to find new electrolyte materials that allow the reduction of the operating temperature of SOFCs. Ceria-based ceramics have been regarded as the most promising electrolytes for intermediate-temperature SOFCs, since their ionic conductivity is higher than that of the zirconia-based electrolytes traditionally used in SOFCs [1,2]. The ionic conductivity of ceria-based electrolytes doped with various dopants (e.g., Ca^{2+}, Sr^{2+}, Y^{3+}, La^{3+}, Gd^{3+}, and Sm^{3+}) at different dopant concentrations, has been extensively investigated [3–6]. Of these various ceria-based electrolytes, Gd^{3+}- or Sm^{3+}-doped ceria ceramics have the highest conductivity due to the smallest association enthalpy between the dopant cation and the oxygen vacancy in the fluorite lattice [7,8]. However, one of the main drawbacks of ceria-based materials is that they are difficult to densify fully below 1500 °C and to have nanostructure due to fast grain growth during sintering by conventional sintering method [9,10]. It has been reported that some transition metal oxides, such as MnO_2, Fe_2O_3, and Co_3O_4, are very effective sintering aids for densification of ceria-based samples [11,12].

Nanostructured materials have been widely investigated because they have a wide functional diversity and exhibit enhanced or different properties compared with bulk materials [13]. Particularly, in the case of nanostructured ceramics, the presence of a large fraction of grain boundaries can lead to unusual or better mechanical, electrical, optical, sensing, magnetic, and biomedical properties [14–19]. In recent days, nanocrystalline powders have been developed by co-precipitation, the thermochemical and thermomechanical process named as the spray conversion process (SCP), and high-energy milling [20,21]. The grain size in sintered materials, however, becomes much larger than that in pre-sintered powders due to a fast grain growth during conventional sintering process. Even though the initial particle size is less than 100 nm, the grain size increases rapidly up to 500 nm or larger during the conventional sintering [22]. Therefore, controlling grain growth during sintering is one of the keys to the commercial success of nanostructured materials. In this regard, the pulsed current activated sintering (PCAS) method which can make dense materials within 2 min has been shown to be effective in achieving this goal [23].

---

* Corresponding author at: Division of Advanced Materials Engineering and the Research Center of Industrial Technology, College of Engineering, Chonbuk National University, 664-14 Deokjin-dong 1-ga, Deokjin-gu, Jeonju, Jeonbuk 561-756, Republic of Korea. Tel.: +82 63 270 2381;
fax: +82 63 270 2386.
E-mail address: ijshon@chonbuk.ac.kr (I.-J. Shon).

0272-8842/$34.00 © 2008 Elsevier Ltd and Techna Group S.r.l. All rights reserved.
doi:10.1016/j.ceramint.2008.06.017

In this work, we report the fabrication of the nanosized $Ce_{0.8}Gd_{0.2}O_{2-\delta}$ powders and the sintering properties of the Fe_2O_3 added $Ce_{0.8}Gd_{0.2}O_{2-\delta}$ materials with nanostructure using PCAS method under high pressure. We have also investigated the effect of Fe_2O_3 on the mechanical properties and ionic conductivity of $Ce_{0.8}Gd_{0.2}O_{2-\delta}$ electrolyte.

2. Experimental procedure

Nanopowders of $Ce_{0.8}Gd_{0.2}O_{2-\delta}$ and Fe_2O_3 were made by co-precipitation method using diluted ammonia as precipitant. High purity (>99.99%) reagents $Ce(NO_3)_3{\cdot}6H_2O$, $Gd(NO_3)_3{\cdot}6H_2O$ and Fe $(NO_3)_3{\cdot}6H_2O$ were used as starting materials. $Ce_{0.8}Gd_{0.2}O_{2-\delta}$ and Fe_2O_3 powders were milled in a Universal Mill with a ball-to-powder weight ratio of 6:1. Milling was done in polyethylene bottles using zirconia balls and was performed at a horizontal rotation velocity of 250 rpm for 24 h.

The powder was placed in a graphite die (outside diameter, 45 mm; inside diameter, 20 mm; and height, 40 mm) and then introduced into the PCAS system made by Eltek in South Korea, shown schematically in Fig. 1. The PCAS apparatus consists of an 18 V, 2800 A DC power supply which provides a pulsed current with 20 μs on time and 10 μs off time through the sample and die, and a 50-kN uniaxial press. The system was first evacuated and then a uniaxial pressure of 80 MPa was applied. A DC current was then activated. Sample shrinkage is monitored in real time by a linear gauge measuring the vertical displacement and temperatures were measured by a pyrometer focused on the surface of the graphite die. Depending on heating rate, the electrical and thermal conductivities of the compact, and its relative density, a difference in temperature between the surface and the center of the sample exists. The sample was sintered at 1080 °C with heating rate of 200 °C/min. At the end of the process, the current was turned off and the sample was allowed to cool to room temperature. The process was carried out under a vacuum of 40 mTorr.

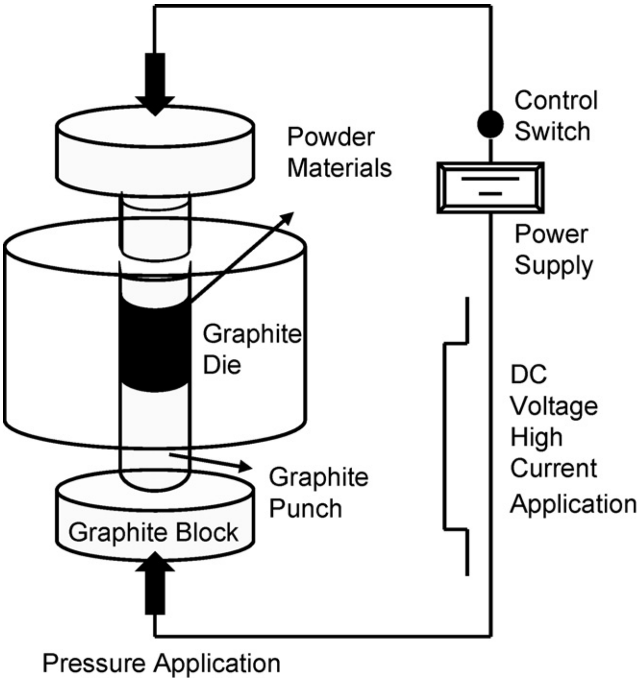

Fig. 1. Schematic diagram of apparatus for pulsed current activated sintering (PCAS).

The relative densities of the synthesized sample were measured by the Archimedes method. Microstructural information was obtained from fracture surface of product samples. Compositional and microstructural analyses of the products were carried out by X-ray diffraction (XRD), scanning electron microscopy (SEM) with energy dispersive X-ray analysis (EDAX) and field-emission scanning electron microscopy (FE-SEM). Vickers hardness was measured by performing indentations at load of 500 g and a dwell time of 15 s on the samples. After polishing with SiC paper, Pt was coated on the both sides of the sintered pellets. The ionic conductivity was measured from 300 to 600 °C in air using a two-probe impedance spectroscopy (Zahner IM6, Germany) in the frequency range of 100 mHz to 3 MHz with the voltage amplitude of 50 mV.

3. Results and discussion

3.1. Powder characterization

Fig. 2 shows FE-SEM image and TEM image of the precipitated $Ce_{0.8}Gd_{0.2}O_{2-\delta}$ powder calcined at 600 °C for 1 h in air. XRD results (Fig. 3) showed that all the peaks of the powder calcined at 600 °C correspond to the fluorite structure of CeO_2 (PDF card number: 34-0394). The lattice parameter of the sample calcined at 600 °C was determined to be 0.5427 nm using the least square refinement method. This value agreed well with the theoretical lattice parameter of the fluorite structure of CeO_2 (theoretical lattice parameter, $a = 0.5411$ nm). There is a very slight difference between the calculated and theoretical lattice parameter due to the substitution of Ce^{4+} by Gd^{3+} in the fluorite structure of CeO_2.

The grain size and the internal strain are calculated by Stokes and Wilson's formula [24],

$$b = b_d + b_e = \frac{k\lambda}{d\cos\theta} + 4\varepsilon\tan\theta \qquad (1)$$

where b is the full width at half-maximum (FWHM) of the diffraction peak after instrument correction; b_d and b_e are FWHM caused by small grain size and internal stress, respectively; K is constant as 0.9; λ is wavelength of the X-ray radiation; d and ε are grain size and internal stress, respectively; and θ is the Bragg angle. b and b_s follow Cauchy form with the relationship: $B_0 = b + b_s$, where B_0 and b_s are FWHM of broadened Bragg peaks and the standard sample's Bragg peaks, respectively. The average grain size $Ce_{0.8}Gd_{0.2}O_{2-\delta}$ measured by Stoke–Wilson equation was about 12 nm.

3.2. Densification behavior of $Ce_{0.8}Gd_{0.2}O_{2-\delta}$

The variations in shrinkage displacement and temperature of the surface of the graphite die with heating time during the processing of $Ce_{0.8}Gd_{0.2}O_{2-\delta}$ doped with different concentration of Fe_2O_3 under 80 MPa pressure are shown in Fig. 4. As the

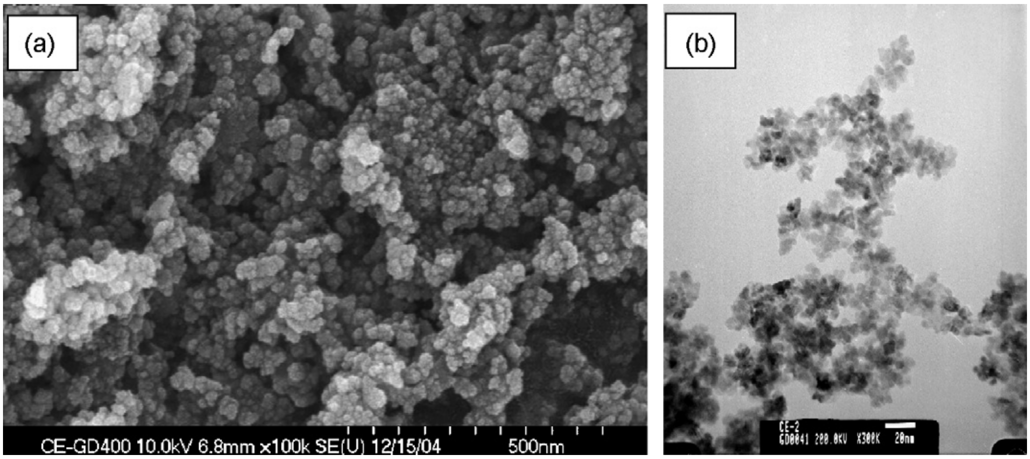

Fig. 2. FE-SEM image (a) and TEM image (b) of $Ce_{0.8}Gd_{0.2}O_{2-\delta}$ powder synthesized by co-precipitation method.

pulsed current was applied, the shrinkage displacement increased with temperature and Fe_2O_3 doping is extremely effective in promoting the densification of $Ce_{0.8}Gd_{0.2}O_{2-\delta}$ when exceeding a dopant concentration of 0.5 mol%. Fig. 5 shows the density and grain size of $Ce_{0.8}Gd_{0.2}O_{2-\delta}$ as a function of Fe_2O_3 content when the sample was sintered at 1080 °C with a heating rate of 200 °C/min under pressure of 80 MPa. Relative density and grain size increased with increasing Fe_2O_3 content up to 1 mol% and then decreased with further addition of Fe_2O_3. Meanwhile, as shown in Fig. 6, the average size of grains determined by linear intercept method were about 100, 850, 1100, 950, and 620 nm for $Ce_{0.8}Gd_{0.2}O_{2-\delta}$ with addition of 0, 0.5, 1, 2, and 3 mol%, respectively.

Fig. 7 shows XRD patterns of the specimens with various Fe_2O_3 contents. The shifts toward high 2θ angle were shown with Fe_2O_3 addition up to 1 mol%, but above 1 mol%, the peaks were not shifted further. The lattice constants calculated from XRD patterns as a function of Fe_2O_3 content are shown in Fig. 8. The lattice constant decreased with increasing Fe_2O_3 content up to 1 mol%, but the value became almost constant when the content of Fe_2O_3 was over 1 mol%. This decrease will be due to the substitution of smaller Fe^{3+} ions for Ce^{4+} in the

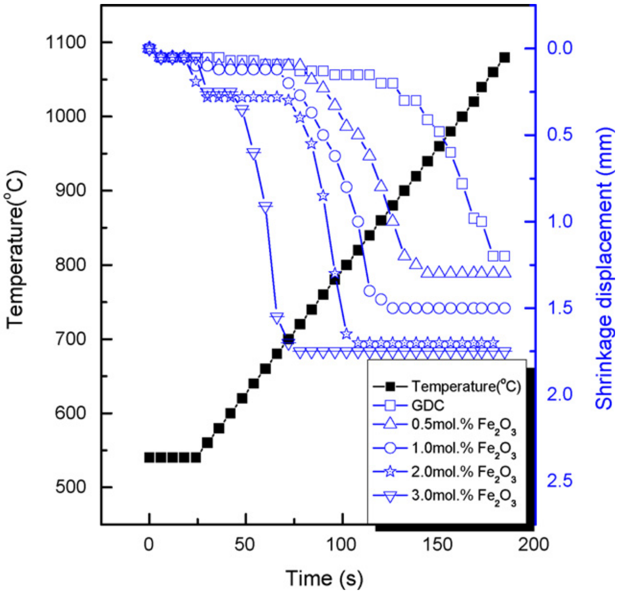

Fig. 4. Variation of temperature and shrinkage displacement with heating time during PCAS of Fe_2O_3 added $Ce_{0.8}Gd_{0.2}O_{2-\delta}$.

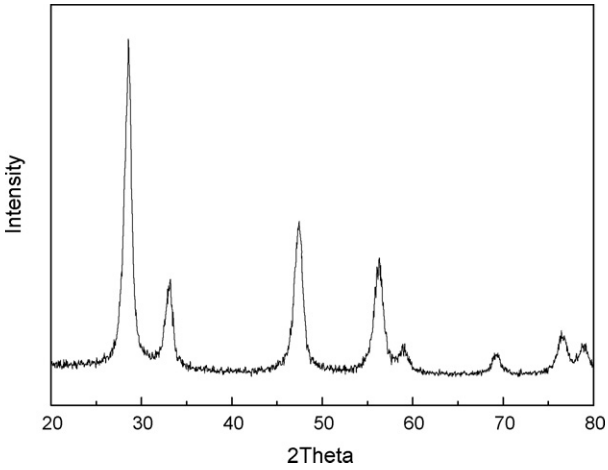

Fig. 3. X-ray diffraction pattern of $Ce_{0.8}Gd_{0.2}O_{2-\delta}$ powder synthesized by co-precipitation method.

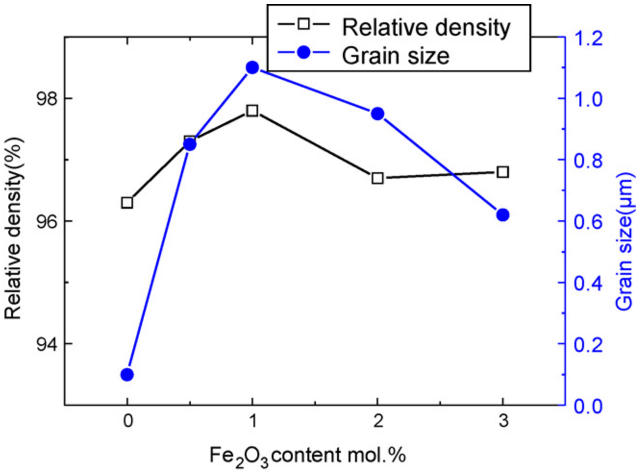

Fig. 5. Relative densities and grain sizes of $Ce_{0.8}Gd_{0.2}O_{2-\delta}$ as a function of Fe_2O_3 content.

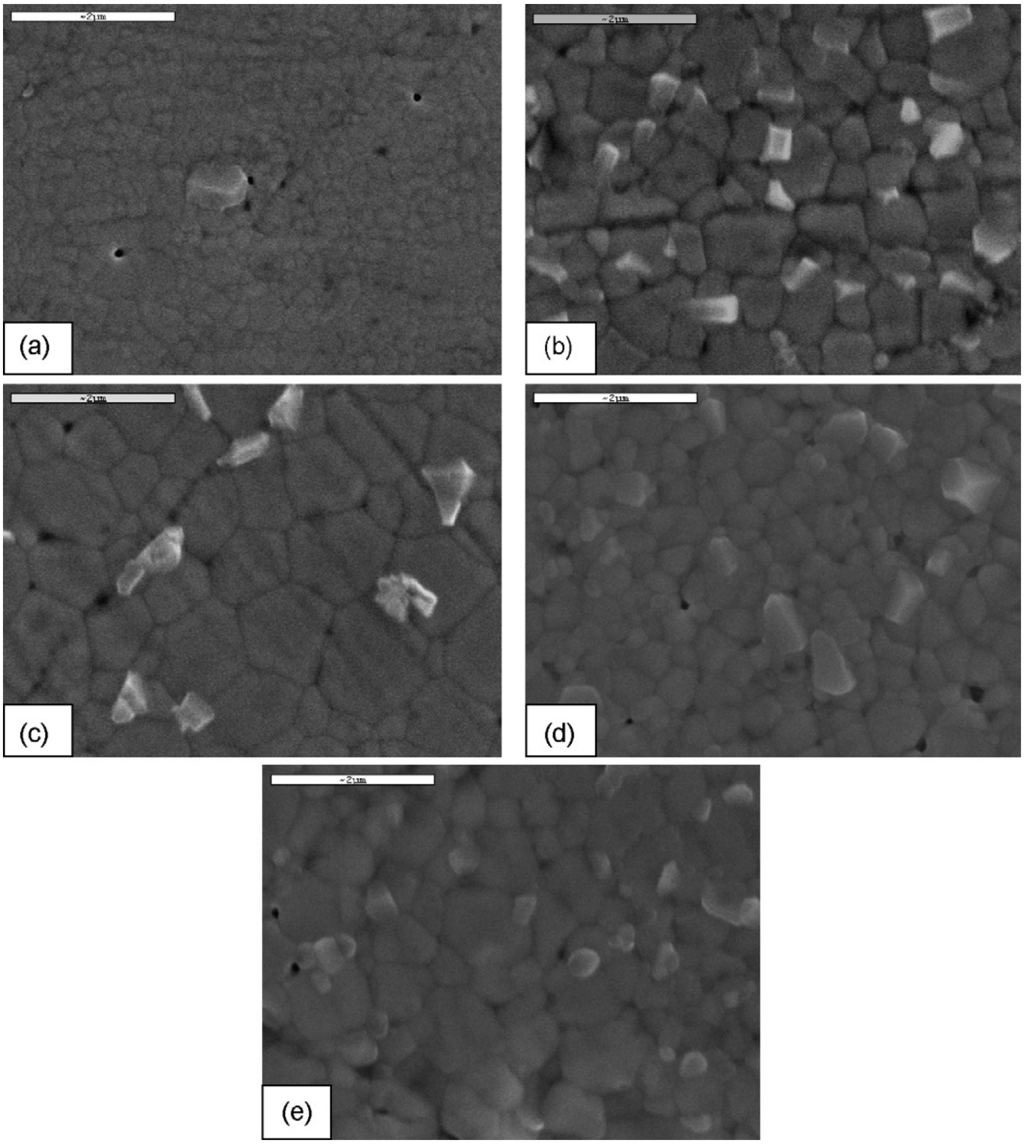

Fig. 6. SEM images of the thermally etched $Ce_{0.8}Gd_{0.2}O_{2-\delta}$ with various Fe_2O_3 contents of (a) 0 mol%, (b) 0.5 mol%, (c) 1 mol%, (d) 2 mol%, and (e) 3 mol%.

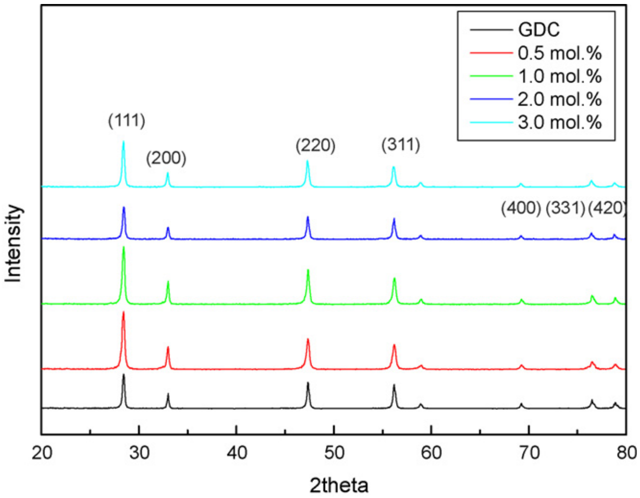

Fig. 7. X-ray diffraction patterns of sintered $Ce_{0.8}Gd_{0.2}O_{2-\delta}$ with various Fe_2O_3 contents.

CeO_2 structure. Thus the solubility limit of Fe_2O_3 in Fe_2O_3-doped CeO_2 is estimated to be 1 mol%. The addition of Fe_2O_3 in a CeO_2 system would lead to the formation of oxygen vacancies because of charge compensation. It is expected that these oxygen vacancies enhance the densification rate and promote the grain boundary mobility. Moreover, the addition of Fe_2O_3 may induce the large distortion of the surrounding lattice because Fe^{3+} ions are much smaller than Ce^{4+} ions. It is also expected that the lattice distortion promotes the grain boundary mobility due to the effect of severely undersized dopant [25]. However, at a higher Fe_2O_3 content over the solubility limit, excess Fe_2O_3 is precipitated. The precipitates inhibit the grain growth and lead to the decrease in grain size by a pinning effect.

3.3. Ionic conductivity of $Ce_{0.8}Gd_{0.2}O_{2-\delta}$

Fig. 9 shows both grain interior and grain boundary conductivities of $Ce_{0.8}Gd_{0.2}O_{2-\delta}$ with addition of Fe_2O_3. The

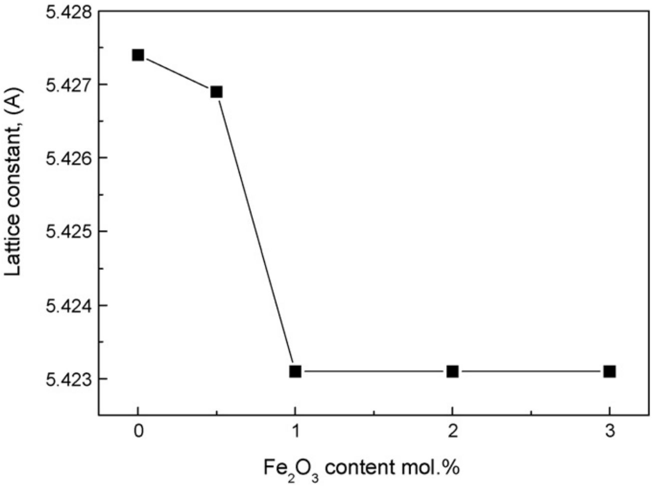

Fig. 8. Lattice constant of $Ce_{0.8}Gd_{0.2}O_{2-\delta}$ as a function of Fe_2O_3 content.

grain boundary conductivity is one order of magnitude lower than the grain interior conductivity. In previous studies, it was assumed that grain boundary resistance is the result of a siliceous phase [26]. Recently, however, it has been reported that the grain boundary conductivity of samples with impurity-free grain boundaries is still about two orders of magnitude lower than bulk or grain interior [27]. It has also been suggested that oxygen vacancy depletion can be affected by dopant ion segregation [28].

Both grain interior and grain boundary conductivity of $Ce_{0.8}Gd_{0.2}O_{2-\delta}$ increased with addition of Fe_2O_3. The increase in conductivity may be contributed to an increase in the relative density and the amount of oxide ion vacancy within the solubility limit of Fe_2O_3.

The ionic conductivity has been fitted as a function of temperature following the Arrhenius law:

$$\sigma = \left(\frac{\sigma_0}{T}\right)\exp\left(-\frac{E_a}{k_B T}\right) \tag{2}$$

where E_a is the activation energy for ionic migration, k_B is the Boltzmann constant, and σ_0 the pre-exponential factor is a constant related to the density of carriers (in this case, oxide vacancies). Figs. 10 and 11 show the Arrhenius plots of grain interior and grain boundary conductivity of $Ce_{0.8}Gd_{0.2}O_{2-\delta}$ with Fe_2O_3 content, respectively. There is no great difference in activation energy with Fe_2O_3 content, as shown in Fig. 12. This result is in accordance with the previous reports [11,29]. The activation energies of grain interior and grain boundary of $Ce_{0.8}Gd_{0.2}O_{2-\delta}$ calculated from Eq. (2) are 0.71 and 1.06 eV, respectively.

3.4. Mechanical properties of $Ce_{0.8}Gd_{0.2}O_{2-\delta}$

In order to investigate the mechanical properties, Vickers hardness and fracture toughness measurements with a 500-g load and 15 s dwell time were carried out on the polished sections of the $Ce_{0.8}Gd_{0.2}O_{2-\delta}$ samples densified under 80 MPa with a heating rate of 200 °C/min at 1080 °C. Fracture toughness was calculated from cracks produced by indentations under large loads. The length of these cracks permits an estimation of the fracture toughness of the materials [30,31] by means of the expression:

$$K_{IC} = 0.204\left(\frac{c}{a}\right)^{-3/2} H_v a^{1/2} \tag{3}$$

where c is the trace length of the crack measured from the center of the indentation, a is the half of average length of two indent diagonals, and H_v is the hardness.

The results of mechanical properties are shown in Fig. 13. Generally, the hardness tends to decrease with increase in grain size. Although the grain size increases with Fe_2O_3 content (Fig. 6), the hardness increases slightly with increasing Fe_2O_3 content. It might be attributed to an increase in relative density. The relative density increases with increasing Fe_2O_3 content as shown in Fig. 5. However, there seems to be no great difference in mechanical properties with Fe_2O_3 content. The hardness and fracture toughness of $Ce_{0.8}Gd_{0.2}O_{2-\delta}$ sintered at 1080 °C is about 815 kg/mm^2 and 2.1 MPa m$^{1/2}$, respectively.

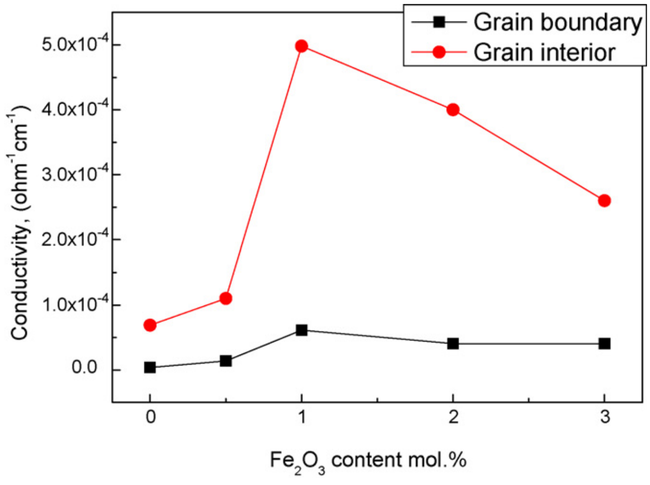

Fig. 9. Variation of grain interior and grain boundary conductivities of $Ce_{0.8}Gd_{0.2}O_{2-\delta}$ at 350 °C as a function of Fe_2O_3 content.

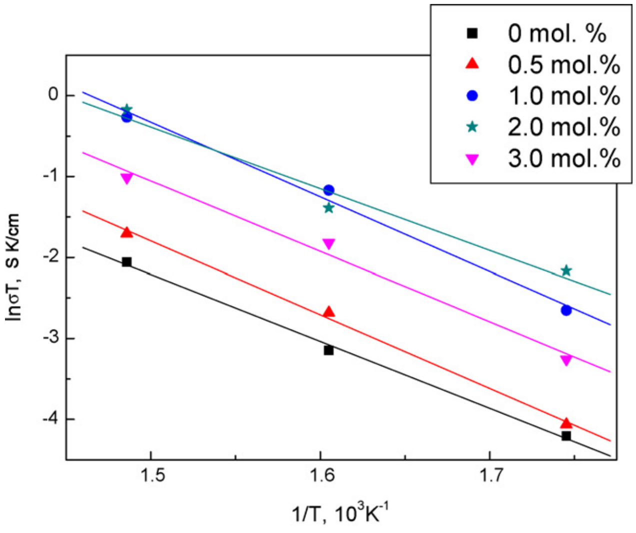

Fig. 10. Arrhenius plots of grain interior conductivity of $Ce_{0.8}Gd_{0.2}O_{2-\delta}$ as a function of Fe_2O_3 content.

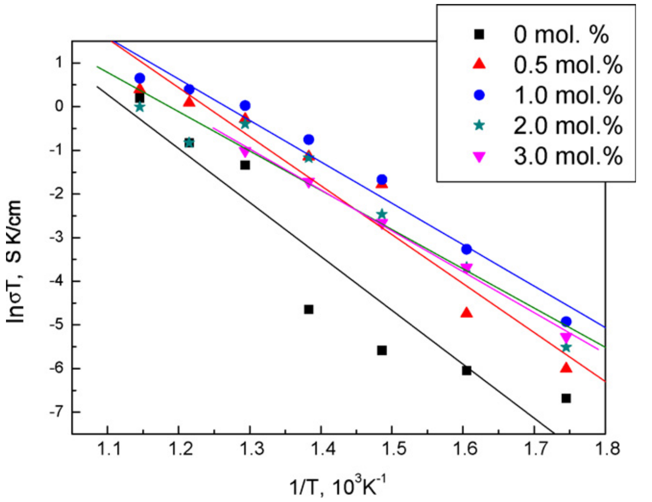

Fig. 11. Arrhenius plots of grain boundary conductivity of $Ce_{0.8}Gd_{0.2}O_{2-\delta}$ as a function of Fe_2O_3 content.

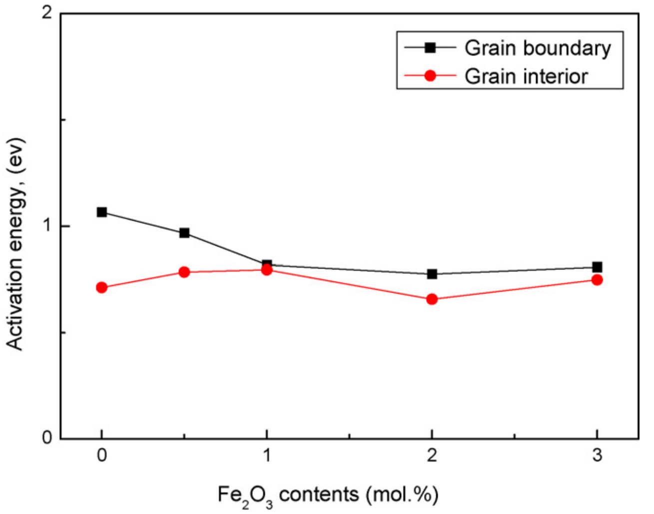

Fig. 12. Variation of activation energies of $Ce_{0.8}Gd_{0.2}O_{2-\delta}$ as a function of Fe_2O_3 content.

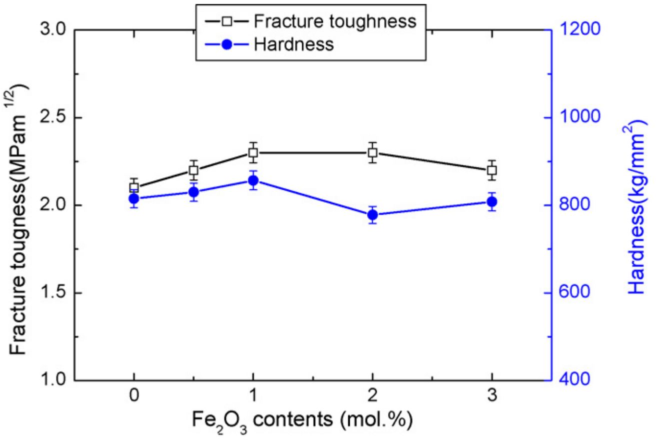

Fig. 13. Variation of hardness and fracture toughness of $Ce_{0.8}Gd_{0.2}O_{2-\delta}$ as a function of Fe_2O_3 content.

4. Summary

Using the PCAS method, the densification of nanostructured $Ce_{0.8}Gd_{0.2}O_{2-\delta}$ was accomplished from nanopowder of $Ce_{0.8}Gd_{0.2}O_{2-\delta}$. The relative density of the $Ce_{0.8}Gd_{0.2}O_{2-\delta}$ was 96.3% with the applied pressure of 80 MPa and the pulsed current. Relative density and grain size increased with increasing Fe_2O_3 content up to 1 mol% and then decreased with further addition of Fe_2O_3. Grain interior conductivity and grain boundary conductivity of $Ce_{0.8}Gd_{0.2}O_{2-\delta}$ slightly increased with addition of Fe_2O_3. The grain boundary conductivity is less than one order of magnitude smaller than the grain bulk conductivity. The activation energies of grain interior and grain boundary of $Ce_{0.8}Gd_{0.2}O_{2-\delta}$ are 0.71 and 1.06 eV, respectively. The hardness and fracture toughness of $Ce_{0.8}Gd_{0.2}O_{2-\delta}$ sintered at 1080 °C are about 815 kg/mm^2 and 2.1 MPa m$^{1/2}$, respectively. There is no great difference in mechanical properties with Fe_2O_3 content.

References

[1] J. Maier, Nano-sized mixed conductors (aspects of nano-ionics. Part III), Solid State Ionics 148 (3–4) (2002) 367–374.
[2] J. Schoonman, Nanoionics, Solid State Ionics 157 (1–4) (2003) 319–326.
[3] R.N. Blumenthal, F.S. Brugner, J.E. Garnier, The electrical conductivity of CaO-doped nonstoichiometric cerium dioxide from 700 to 1500 °C, Journal of the Electrochemical Society 120 (9) (1973) 1230–1237.
[4] H. Yahiro, K. Eguchi, H. Arai, Ionic conduction and microstructure of the ceria–strontia system, Solid State Ionics 21 (1) (1986) 37–47.
[5] J. Faber, C. Geoffroy, A. Roux, A. Sylvestre, P. Abelard, A systematic investigation of the dc electrical conductivity of rare-earth doped ceria, Applied Physics A: Materials Science & Processing 49 (3) (1989) 225–232.
[6] G.B. Balazs, R.S. Glass, ac Impedance studies of rare earth oxide doped ceria, Solid State Ionics 76 (1–2) (1995) 155–162.
[7] R. Gerhard-Anderson, A.S. Nowick, Ionic conductivity of CeO_2 with trivalent dopants of different ionic radii, Solid State Ionics 5 (1981) 547–550.
[8] J.A. Kilner, Fast anion transport in solids, Solid State Ionics 8 (3) (1983) 201–207.
[9] T. Kudo, H. Obayashi, Oxygen ion conduction of the fluorite-type $Ce_{1-x}Ln_xO_{2-x/2}$ (Ln = lanthanoid element), Journal of the Electrochemical Society 122 (1) (1975) 142–147.
[10] H. Yahiro, K. Eguchi, H. Arai, High temperature fuel cell with ceria–yttria solid electrolyte, Journal of the Electrochemical Society 135 (8) (1998) 2077–2080.
[11] T.S. Zhang, J. Ma, Y.J. Leng, S.H. Chan, P. Hing, J.A. Kilner, Effect of transition metal oxides on densification and electrical properties of Si-containing $Ce_{0.8}Gd_{0.2}O_{2-\delta}$ ceramics, Solid State Ionics 168 (1–2) (2004) 187–195.
[12] C. Kleinlogel, L.J. Gauckler, Sintering and properties of nanosized ceria solid solutions, Solid State Ionics 135 (1–4) (2000) 567–573.
[13] H. Gleiter, Nanostructured materials: state of the art and perspectives, Nanostructured Materials 6 (1–4) (1995) 3–14.
[14] J. Karch, R. Birringer, H. Gleiter, Ceramics ductile at low temperature, Nature 330 (1987) 556–558.
[15] A.M. George, J. Iniguez, L. Bellaiche, Anomalous properties in ferroelectrics induced by atomic ordering, Nature 413 (2001) 54–57.
[16] D. Hreniak, W. Strek, Synthesis and optical properties of Nd^{3+}-doped $Y_3Al_5O_{12}$ nanoceramics, Journal of Alloys and Compounds 341 (1–2) (2002) 183–186.
[17] C. Xu, J. Tamaki, N. Miura, N. Yamazoe, Grain size effects on gas sensitivity of porous SnO_2-based elements, Sensors and Actuators B: Chemical 3 (2) (1991) 147–155.
[18] D.G. Lamas, A. Caneiro, D. Niebieskikwiat, R.D. Sanchez, D. Garcia, B. Alascio, Transport and magnetic properties of nanocrystalline $La_{2/3}Sr_{1/}$

${}_3MnO_3$ powders synthesized by a nitrate–citrate gel-combustion process, Journal of Magnetism and Magnetic Materials 241 (2–3) (2002) 207–213.

[19] E.S. Ahn, N.J. Gleason, A. Nakahira, J.Y. Ying, Nanostructure processing of hydroxyapatite-based bioceramics, Nano Letters 1 (3) (2001) 149–153.

[20] Z. Fang, J.W. Eason, Study of nanostructured WC–Co composites, International Journal of Refractory Metals and Hard Materials 13 (5) (1995) 297–303.

[21] A.I.Y. Tok, L.H. Luo, F.Y.C. Boey, Carbonate co-precipitation of Gd_2O_3-doped CeO_2 solid solution nano-particles, Materials Science and Engineering A 383 (2) (2004) 229–234.

[22] M. Sommer, W.D. Schubert, E. Zobetz, P. Warbichler, On the formation of very large WC crystals during sintering of ultrafine WC–Co alloys, International Journal of Refractory Metals and Hard Materials 20 (1) (2002) 41–50.

[23] H.C. Kim, I.J. Shon, J.K. Yoon, J.M. Doh, Consolidation of ultra fine WC and WC–Co hard materials by pulsed current activated sintering and its mechanical properties, International Journal of Refractory Metals and Hard Materials 25 (1) (2007) 46–52.

[24] F.L. Zhang, C.Y. Wang, M. Zhu, Nanostructured WC/Co composite powder prepared by high energy ball milling, Scripta Materialia 49 (11) (2003) 1123–1128.

[25] P.L. Chen, I.W. Chen, Grain growth in CeO_2: dopant effects, defect mechanism, and solute drag, Journal of the American Ceramic Society 79 (7) (1996) 1793–1800.

[26] S.P.S. Badwal, J. Drennan, The effect of thermal history on the grain boundary resistivity of Y–TZP materials, Solid State Ionics 28–30 (2) (1998) 1451–1455.

[27] M. Aoki, Y.M. Chiang, I. Kosacki, J.R. Lee, H. Tuller, Y. Liu, solute segregation and grain-boundary impedance in high-purity stabilized zirconia, Journal of the American Ceramic Society 79 (5) (1996) 1169–1180.

[28] X. Guo, Size dependent grain-boundary conductivity in doped zirconia, Computational Materials Science 20 (2) (2001) 168–176.

[29] T.S. Zhang, J. Ma, Y.J. Leng, S.H. Chan, P. Hing, J.A. Kilner, Iron oxide as an effective sintering aid and a grain boundary scavenger for ceria-based electrolytes, Solid State Ionics 167 (1–2) (2004) 203–207.

[30] D.Y. Oh, H.C. Kim, J.K. Yoon, I.J. Shon, One step synthesis of dense $MoSi_2$–SiC composite by high-frequency induction heated combustion and its mechanical properties, Journal of Alloys and Compounds 395 (1–2) (2005) 174–180.

[31] N. Koichi, Indentation microfracture of ceramics, Ceramics 20 (1985) 1218–1224.